Simple Hydrothermal Synthesis of g-C3N4/Ni9S8 Composites for Efficient Photocatalytic H2 EvolutionSimple Hydrothermal Synthesis of g-C3N4/Ni9S8 Composites for Efficient Photocatalytic H2 Evolution

Ao Li
China University of Geosciences Beijing https://orcid.org/0000-0002-7382-0179
Zhijian Peng
China University of Geosciences
Xiuli Fu (xiulifu@bupt.edu.cn)
Beijing University of Posts and Telecommunications

Research Article

Keywords: g-C3N4 photocatalyst, Ni9S8 co-catalyst, High conductivity, Hydrogen evolution reaction

Posted Date: March 6th, 2021

DOI: https://doi.org/10.21203/rs.3.rs-270784/v1

Version of Record: A version of this preprint was published at Journal of Materials Science: Materials in Electronics on July 28th, 2021. See the published version at https://doi.org/10.1007/s10854-021-06678-9.

Abstract

The prompt recombination between photogenerated electrons and holes is the common problem for improving the hydrogen evolution properties of a photocatalyst, which could be solved greatly by composite co-catalysis. Herein, a simple hydrothermal reaction was utilized to prepare g-C_3N_4/Ni_9S_8 composite photocatalysts. Through electroless nickel plating, Ni_9S_8 nanostructure was homogeneously grown onto the g-C_3N_4 surface by using sodium hypophosphite as reducing agent. With the optimum amount of Ni_9S_8, the acquired g-C_3N_4/Ni_9S_8 composite compared with the raw g-C_3N_4 which has an excellent increase in hydrogen evolution rate under visible light irradiation. Its rate of hydrogen evolution measured at 7 degrees Celsius was 355.7 $\mu mol \cdot g^{-1} \cdot h^{-1}$, being 21.2 time that of raw g-C_3N_4. The mechanism for the hydrogen evolution reaction over the present g-C_3N_4/Ni_9S_8 composite photocatalysts was discussed in detail.

1. Introduction

Nowadays, human beings are suffering from energy shortage, environmental pollution and extreme climate, because the increasing large-scale use of fossil energy will cause the depletion of easily available energy sources, which gives a pessimistic perspective for the reserve of fossil energy, together with a lot of waste gases and greenhouse gases, which have great impact on the earth's ecology [1-x]. Therefore, the development of new energy is very urgent for mankind. Hydrogen energy, as a pearl of new energy, has attracted much attention because of its high calorific value, no carbon emission and facile recyclability [2]. And since 1972 when Fujishima and Honda discovered that TiO_2 could decompose water into hydrogen and oxygen under ultraviolet light [3], it seems for human beings to find a shortcut to solve the energy problem once and for all. Thus now photocatalysis is such an exciting technology that attracts numerous researchers to study.

It is soon recognized by scientists that photocatalysis is based on the photoelectric conversion of semiconductors, and ultimately the conversion of light into chemical energy [4]. Therefore, the exploration of semiconductor photocatalysts has been rapidly launched. Today, many photocatalytic semiconductors such as ZnO, Ga_2O_3, $SrTiO_3$ and ZnS [5-8] have been found to be similar with TiO_2 in photocatalytic decomposition of water. However, these semiconductor photocatalysts can only respond to ultraviolet light because of their wide bandgap. To effectively make use of visible light, in which the sunlight (containing almost 96% visible light) is an inexhaustible energy source for human beings, researchers have developed CdS, MoS, Cu_2O and many other narrow bandgap semiconductors for photocatalytic hydrogen evolution [9-11]. But their poor photochemical stability, heavy metal pollution on water and less earth reserves limit their large-scale application [12].

In 2009, Wang *et al.* first found that g-C_3N_4 has the ability of photocatalytic decomposition of water under visible light [13]. Such ability of this kind of organic semiconductors has soon aroused the great interest of scientists. In literature, a large number of studies have shown that g-C_3N_4 owns a bandgap of roughly

2.78 eV, which can respond to light sources with wavelength below 460 nm [14]. At the same time, it has the advantages of strong photochemical stability, low cost, easy availability, non-toxicity and pollution free for environment [15]. In spite of these virtues, however, there are a large number of intrinsic defects in such organic semiconductors, which make the photogenerated carriers over g-C_3N_4 under light rapidly conform to these defects, thus seriously degrading its photocatalytic activity [12].

To reduce the recombination of photogenerated carriers (holes and electrons) in photocatalysts, co-catalysis is an excellent solution [16]. For example, noble metals like Au, Pt, Pd, Rh and so on have excellent catalytic effect due to their unique surface plasmon effect, which can also serve as good co-catalysts [17]. Regrettably, noble metals cannot widely be used in photocatalytic industry due to their high cost and scarce reserves. Therefore, it is very important to find low-cost co-catalysts for photocatalytic hydrogen evolution. In addition, by combining different semiconductor photocatalysts together to form a built-in electric field, photogenerated electrons are easily transferred from the optical semiconductor to the co-catalytic semiconductor. At this time, because of the Schottky barrier, the photogenerated electrons are difficult to return to the original photocatalyst, thus the separation of photogenerated carriers is realized [14]. Meanwhile, for this co-catalytic semiconductor, low overpotential and good conductivity are very helpful for hydrogen evolution. Therefore, it is a feasible idea to find a semiconductor with low overpotential and good conductivity to replace noble metals.

In literature, NiS has been regarded as an excellent co-catalyst in photocatalytic hydrogen evolution, and hopefully it can replace noble metals. This is due to the following advantages of NiS: (1) high conductivity due to low bandgap, (2) low surface work function that can effectively reduce the reaction activation energy or over potential, (3) high power conversion efficiency, and (4) easy preparation, low cost as well as environmental friendliness [18]. Therefore, a lot of researches have been executed on the co-catalysis of NiS in photocatalysis, such as CdS/NiS, TiO_2/NiS, g-C_3N_4/NiS and MoO_3/NiS [19-22]. However, since nickel sulfides can exist in different component including NiS, NiS_2, Ni_3S_4, Ni_4S_3, Ni_9S_8 and so forth [23], it is difficult for researchers to study them fully. Among them, Ni_9S_8 is less involved because it is not easily synthesized. As far as we know, no one has reported any composite of Ni_9S_8 and g-C_3N_4. Moreover, Ni_9S_8 has a near zero bandgap compared with NiS, which implies that Ni_9S_8 has better conductivity and is more conducive to the transmission of photogenerated electrons [24]. Therefore, it is much desirable to prepare the composite of g-C_3N_4 and Ni_9S_8 on photocatalytic hydrogen evolution.

In the present work, we adopt a facile green hydrothermal route to grow Ni_9S_8 nanostructures onto the pre-prepared g-C_3N_4 nanosheet, obtaining the g-C_3N_4/Ni_9S_8 composite. In the synthesis of g-C_3N_4/Ni_9S_8 composite, in order to form Ni_9S_8, $NaHPO_2$ was used, which is commonly used in electroless nickel plating, to reduce Ni^{2+} to metal Ni, and then to conduct the redox reaction with S^{2+} to obtain the g-C_3N_4/Ni_9S_8 composite. The results reveal that the as-acquired g-C_3N_4/Ni_9S_8 composite has a uniform dispersion of Ni_9S_8 nanostructures on the g-C_3N_4 nanosheet. Possessing the high conductivity, low surface work function and high electron mobility, the as-acquired composite photocatalyst has excellent photocatalytic performance for hydrogen evolution, presenting a H_2 evolution rate as high as 355.7

mmol·g^{-1}·h^{-1} at 7 ℃. The successful preparation of the present composite will also provide a new perspective for developing other high-performance heterostructure photocatalysts for hydrogen evolution.

2. Experimental

2.1 Raw materials

Sodium hypophosphite (NaH_2PO_2, 99.0%), nickel acetate ($Ni(CH_3COO)_2$, 99.5%), melamine (99.5%), thiourea (CH_4N_2S, 99.5%), ethanol (C_2H_5OH, 99.9%), triethanolamine (TEOA, 99.5%), $H_2PtCl_6·6H_2O$ (99.5%) and Na_2SO_4 (99.5%) were bought from Sinopharm Chemical Reagent Co., Ltd. (Shanghai, China). During the experiments, all the raw materials are used without further treatment.

2.2 Synthesis of g-C_3N_4 particles

Bulk g-C_3N_4 samples were first synthesized by directly heating melamine [25]. Typically, in an open box furnace, a half-covered crucible with 5 g of melamine powder is heated from room temperature to 550 ℃ at a speed of 5 ℃/min, soaking at this temperature for 4 h. Afterwards, the furnace was cooled down to ambient temperature, and then the resultant bulk sample was ground, finally obtaining yellow g-C_3N_4 powders.

2.3 Synthesis of g-C_3N_4/Ni_9S_8 nanocomposites

A facile one-step hydrothermal approach was applied in this work to synthesize the proposed g-C_3N_4/Ni_9S_8 nanocomposites. Typically, in a beak with 50 mL deionized water, 100 mg of the as-obtained g-C_3N_4 powders was homogeneously dispersed through vigorous stirring for 30 minutes under sonicating. Then, in order to obtain g-C_3N_4/Ni_9S_8 composites with different loading amounts of Ni_9S_8, a series of designed amount of nickel acetate (0.05, 0.1, 0.2, 0.3, 0.4, 0.5, 0.7 and 0.9 mmol, respectively) were added into the dispersion solution. And thiourea with an amount of three times that of nickel acetate was mixed in the dispersion solution together. After further strong stirring for 30 minutes, 300 mg sodium hypophosphite was mixed in the solution system. After stirring evenly, the solution was transferred into an autoclave (100 ml) and then kept in an oven at 140 ℃ for 8 h. By simply shutting the electricity of the furnace, it was cooled down to ambient temperature. And then the autoclave was taken out from the oven. The resultant precipitates were collected after centrifuging, washed twice with 30 ml deionized water as well as absolute ethanol respectively, and dried out at 60 ℃ for 8 h. Finally, the proposed, dark blue powders could be acquired.

2.4 Materials characterization

In this work, a Zeiss GEMINISEM 500 field emission scanning electron microscope (FE-SEM, Germany) was first applied to examine the morphology and microstructure of the samples. Then a Thermo ESCALAB MKII X-ray photoelectron spectroscope (XPS, Thermo VG Scientific Ltd., UK) was used to explore their elemental composition and chemical state. With the C1s line (284.8 eV) as reference, the

recorded results were corrected. In order to identify their phase compositions, X-ray diffraction (XRD) analysis was executed (GI-XRD, Japan; Cu Kα radiation, λ= 1.5418 Å). For the analysis, the corresponding scanning rate was set as 4 °/min with 1° of X-ray incidence angle in continuous scanning mode. Finally, with a Varian Cary 5000 UV-vis spectrometer (Agilent, America), the UV-visible absorption spectrum of the samples was collected.

2.5 Evaluation of photocatalytic hydrogen evolution

For the accurate date of hydrogen evolution, in each test 50 mg catalyst was first diffused into 100 ml TEOA aqueous solution with a concentration of 10 vol.%. Then, the prepared reaction mixture was settled in a Perfectlight LabSolar Photocatalytic Hydorogen Evolution System (Beijing, China). The system possesses a Xe lamp (300 W) with an UV cut-off filter (λ ≥ 420 nm) for light source. Afterwards, the system is sealed. Before photocatalytic reaction, the system was first evacuated to a vacuum of -0.1 MPa, and throughout the photocatalytic reaction, the cooling system based on circulating water should work continuously to keep the reaction temperature at 7 ℃. For the reaction, the applied light source was placed 20 cm far from the reaction vessel, and the area for effective irradiation was measured as 12.57 cm^2. During the reaction, the generated gas was characterized by a gas chromatography (GC-7900, Xuansheng Scientific Instrument Co. Ltd, Shanghai, China) on-line with nitrogen as carrier gas. Additionally, each of the cyclic tests for photocatalytic hydrogen evolution was executed for 3 hours and the gas products were taken for characterization every half an hour. After one round of tests, the reactor will be evacuated for 30 minutes, and then the subsequent round of tests is repeated without changing the reaction liquid.

2.6 Photoelectrochemical characterization

For each photoelectrochemical test, a working electrode was first fabricated, for which 50 μL ink prepared from 5 mg sample, 500 μL absolute ethanol together with 20 μL Nafion solution (5 wt.%) was coating onto a FTO glass substrate, finally forming an electrode with a size of 1 cm^2. The electrolyte is 0.2 M Na_2SO_4 aqueous solution.

The measurement on transient photocurrents was carried out by a standard three-electrode system on an electrochemical workstation (CHI 660E, Chenhua Instrument, Shanghai, China). For the measurement, a piece of Pt foil was used as counter electrode, Ag/AgCl (saturated KCl) was used as reference electrode, and the visible light (λ ≥ 420 nm) was provided by a Xe lamp (300 W) using an UV cut-off filter. Prior to the tests, the system should be degassed by high-purity N_2 gas for about 30 minutes.

The samples' electrochemical impedance spectra (EIS) were recorded with the same parameters as those in measuring transient photocurrents. During the EIS tests, the frequency falls in the range of 0.01-100000 Hz, and the applied AC amplitude is 5 mV (vs. Ag/AgCl).

3. Results And Discussion

3.1 Photocatalytic performance for H_2 evolution

To reveal the photocatalytic activity of the proposed g-C_3N_4/Ni_9S_8 composite, all the samples were tested for hydrogen evolution under the irradiation of visible light at 7 °C. Firstly, a series of samples prepared with different Ni/g-C_3N_4 feed molar ratios were tested to determine the optimal sample. Fig. 1a compares their hydrogen evolution rates (HERs). As can be seen in this figure, with the increase of feeding amount of nickel source, the HER value of the acquired samples can be improved. When the Ni/g-C_3N_4 feed molar ratio was 0.2, their HER value reached the highest, which was 355.7 $\mu mol \cdot g^{-1} \cdot h^{-1}$. With more nickel source added, the performance of the obtained photocatalysts declined again, possibly because that the excessive addition of nickel source would lead to a large amount of nickel sulfides coating on g-C_3N_4, which would hinders the absorption of light by g-C_3N_4, thus reducing the hydrogen evolution efficiency of the catalysts. So, the optimal Ni/g-C_3N_4 feed molar ratio for the present composite samples is 0.2. In Fig. 1b, the HER values of the raw g-C_3N_4, the pure Ni_9S_8, the raw g-C_3N_4 which loaded with Pt (1 wt.%) and the optimal g-C_3N_4/ Ni_9S_8 composite are compared. Among them, the sample of g-C_3N_4 with Pt was obtained by adding 1 wt.% chloroplatinic acid into the photocatalytic reaction cell and irradiating it with a 300 W xenon lamp for 30 min. As is seen in the figure, the sample of raw g-C_3N_4 only has a very small HER and the pure Ni_9S_8 has no detectable photocatalytic hydrogen evolution ability. However, the HER value of the optimal composite sample can reach 355.7 $\mu mol \cdot g^{-1} \cdot h^{-1}$. This remarkable value is 21.2 times that of the raw g-C_3N_4, and only 22.1% less than the sample of raw g-C_3N_4 which loaded with Pt (1 wt.%). Therefore, it can be inferred that the compositing between g-C_3N_4 as well as Ni_9S_8 will present a synergistic effect, which can effectively transfer the photogenerated electrons on g-C_3N_4 to Ni_9S_8 through the interface charge transfer effect. And then the electrons on Ni_9S_8 can also combine with H^+ to generate hydrogen, which greatly improves the photocatalytic efficiency of g-C_3N_4. Additionally, in order to determine the stability of the sample, the optimal sample was continuously reacted for 3*6 h in the light reaction cell. It can be seen from the cyclic test results of the composite sample as shown in Fig. 1c that the HER value of the sample has no obvious change after 18 h of cyclic test. Therefore, it can be concluded that the optimal composite has good cycling stability.

3.2 Compositional and structural properties

To elucidate the photocatalytic performance of the acquired samples, their composition and structure were investigated. Firstly, SEM imaging was carried out. Fig. 2a shows typical SEM micrograph of the optimal g-C_3N_4/Ni_9S_8 composite. As is seen, this composite sample has a similar morphology with that of the raw g-C_3N_4 sample. Therefore, the two-dimensional structure of raw g-C_3N_4 is not destroyed in the recombination process. To explore the distribution of nickel sulfides in the sample, EDS mapping scanning was executed in the same area for SEM imaging. And the results are displayed in Fig. 2b-d. It is easily seen that N, Ni as well as S atoms are homogeneously distributed over the sampling area. Therefore, it can be concluded that the nickel sulfides in the obtained composite is uniformly grown onto the g-C_3N_4 surface, rather than a simple mixture of both components. The uniform composition and

structure is one of the reasons why the proposed g-C_3N_4/Ni_9S_8 composite has high photocatalytic activity.

To determine the specimens' phase composition, XRD analysis was carried out. Fig. 3 compares the recorded XRD patterns of the optimal composite, the raw g-C_3N_4 and pure nickel sulfides samples, in which the raw g-C_3N_4 specimen was acquired by the calcination of melamine, while the nickel sulfides sample was obtained under the similar conditions as done for the optimal composite but without the addition of g-C_3N_4. As is seen, the main XRD peaks of the pure nickel sulfides sample can be indexed to orthorhombic Ni_9S_8 phase (JCPDS no.22-1193), while a small amount of hexagonal NiS (JCPDS no.12-0041) can be also identified, indicating that it is a mixture of Ni_9S_8 as the main body with a small amount of hexagonal NiS. The XRD peaks of the raw g-C_3N_4 sample match perfectly with those of its predecessors, confirming its successful synthesis in this work [12]. And in the optimal composite, only the diffraction peaks of g-C_3N_4 and Ni_9S_8 can be identified, which proves that it is a relatively pure composite of g-C_3N_4 and Ni_9S_8.

The elemental composition as well as chemical state of the optimal g-C_3N_4/Ni_9S_8 composite was further detected by XPS analysis. The obtained results are shown in Fig. 4. XPS survey spectroscopy reveals that the optimal g-C_3N_4/Ni_9S_8 sample is composed of C, N, Ni and S, indicating that it is a composite of these elements as expected. The high-resolution C 1s spectrum as exhibited in Fig. 4a presents two distinct peaks at 282.8 and 286.0 eV. Literature survey reveals that the peak at 282.8 eV could be assigned to free carbon, while the one at 286.0 eV should be indexed to the binding energy of C atoms in g-C_3N_4 [26]. The N 1s spectrum (see Fig. 4b) can be fitted into four peaks at 396.5, 397.9, 399.2 and 402.3 eV, respectively. Among them, the three peaks at 396.5, 397.9 and 399.2 eV could be ascribed to the sp^2 hybrid nitrogen in C=N-C group, sp^3 hybrid nitrogen in N-$(C)_3$ structure and nitrogen in amino moiety in g-C_3N_4, respectively, while the one at 402.3 eV is owing to the dangling bond of N on the g-C_3N_4 surface [27]. The Ni 2p spectrum (Fig. 4c) exhibits two main peaks at 853.2 and 860.4 eV, in which the one at 853.2 eV can be attributed to Ni^{2+} in Ni_9S_8, and that at 860.4 eV is assigned to Ni^{2+} in the hydroxyl compound of nickel [24]. However, the phase of hydroxyl compound of nickel could not be identified from the XRD patterns, possibly because its content in the samples were too small. In a word, the main reason for the formation of this binding energy is the hydroxyl hanging bond on the surface of Ni_9S_8 during hydrothermal reaction [18]. Correspondingly, the S 2p spectrum presented in Fig. 4d displays two main peaks at 160.2 and 166.5 eV. The peak at 160.2 eV can be attributed to the S atom in Ni_9S_8 lattice, while that at 166.5 eV may be due to the attachment of some sulphate produced by thiourea hydrolysis on the surface of the sample [24].

In summary, the above-mentioned characterizations reveal that a g-C_3N_4/Ni_9S_8 composite with uniform composition and structure has been successfully synthesized in this work.

The formation mechanism of g-C_3N_4/Ni_9S_8 composite as follow was proposed based on the above experimental results (Fig. 5). In the designed first step, the raw g-C_3N_4 powder is dispersed in deionized water by ultrasonic stirring to form uniformly dispersed g-C_3N_4 nanosheets. After nickel acetate and thiourea joined into the reaction system, because of the negative charges on the g-C_3N_4 nanosheets, Ni^{2+} could be adsorption on the surface of g-C_3N_4, while thiourea could form a complex with Ni^{2+} to slow down the release of Ni^{2+}. In the second step, during the hydrothermal reaction, sodium hypophosphite was first decomposed into PH_3, which could be ionized into H^- with strong reducibility. Then the H^- can reduce Ni^{2+} attached to g-C_3N_4 surface into metal Ni. In the third step, the stable thiourea was thermally decomposed to produce a large amount of S^{2-} and reacted with the metal Ni grown on the g-C_3N_4 surface to obtain the proposed composite in the state full of unsaturated sulfur. Finally, the g-C_3N_4/Ni_9S_8 composite in the state of unsaturated sulfur was obtained. We got this idea by referring to the method of electroless nickel plating [28].

3.3 Photocatalytic mechanism

To clarify the photocatalytic mechanism for H_2 evolution of the as-acquired g-C_3N_4/Ni_9S_8 composite, its photoelectrochemical features were further explored. For comparison, the Ni_9S_8 nanostructure and raw g-C_3N_4 were also investigated. Fig. 6a compares the UV-visible absorption spectrum of the optimal g-C_3N_4/Ni_9S_8 composite with those of raw g-C_3N_4 and Ni_9S_8 nanostructure. It can be seen that the starting point of the absorption edge for the raw g-C_3N_4 is about 440 nm, which is well corresponding to the value reported in literature [29]. However, after g-C_3N_4 was combined with Ni_9S_8, the absorption ability for visible light of the obtained composite was greatly enhanced, while the absorption capacity for ultraviolet and near ultraviolet spectrum below 450 nm was also significantly increased. This result reveals that after the Ni_9S_8 co-catalyst was loaded onto the g-C_3N_4 nanosheets, the optical absorption region of the composite sample could be effectively broadened. The enhanced ability in optical absorption could be owing to the existence of low bandgap black Ni_9S_8 in the g-C_3N_4/Ni_9S_8 composite. Such Ni_9S_8 nanostructures have strong optical absorption to the light with a wavelength from 300 to 800 nm. Furthermore, the bandgaps of the as-acquired, optimal g-C_3N_4/Ni_9S_8 composite together with the raw g-C_3N_4 sample was estimated from their corresponding plots on $(ahv)^2$ versus E_g (see Fig. 6b). As is seen, the Eg values of the as-acquired, optimal g-C_3N_4/Ni_9S_8 composite and the raw g-C_3N_4 are 2.85 and 2.88 eV, respectively. This little difference in their Eg values implies that there is almost no doping effect in the present composite.

Moreover, the transient photocurrents of the raw g-C_3N_4, pure Ni_9S_8 together with the optimal g-C_3N_4/Ni_9S_8 composite are compared in Fig. 7a. We can find out that the prepared raw g-C_3N_4 sample has only 0.3 μA/cm^2 of transient photocurrent, which is far less than that of the optimal composite. This is because the photogenerated electrons and holes are easily recombined with each other in the raw g-C_3N_4 sample. In addition, on the prepared pure Ni_9S_8 nanostructure the detected photocurrent is not distinct,

indicating that although it has strong absorption to the light at the wavelength of 300-800 nm, it can not contribute to the transient photocurrent of the present composite independently. These facts prove that in the present g-C_3N_4/Ni_9S_8 composite, the Ni_9S_8 nanostructure is not a photocatalyst but a co-catalyst for g-C_3N_4. The Ni_9S_8 co-catalyst can boost the segregation of photogenerated electrons and holes, thus increase the efficiency of photogenerated carrier transfer.

Furthermore, the recorded EIS Nyquist curves (see Fig. 7b) reveal that among the three investigated samples, the raw g-C_3N_4 sample possesses the highest intrinsic impedance, indicating that there is a higher charge transfer rate in the composite g-C_3N_4/Ni_9S_8 samples after the loading of Ni_9S_8 onto g-C_3N_4. These phenomena may be due to the homogeneous combination of the relatively low-conductivity g-C_3N_4 nanosheets with the high-conductivity Ni_9S_8 nanostructures.

According to the above-mentioned experimental results, the possible photocatalytic mechanism over the present g-C_3N_4/Ni_9S_8 composite on hydrogen evolution was proposed (see Fig. 8). Under the irradiation of visible light, the photogenerated electron (e^-) will leap into the conduction band (CB) of g-C_3N_4, which will leave hole (H^+) in its valence band (VB). A part of photogenerated electrons could move to the g-C_3N_4 surface and directly reduce H^+ ions in solution to produce H_2. More importantly, due to the close contact between the main body g-C_3N_4 and the high-conductivity Ni_9S_8 nanostructures in the present g-C_3N_4/Ni_9S_8 composite, the built-in electric field is formed after the combination between them. As a result, the photogenerated electrons would easily emigrate to the Ni_9S_8 surface, thus effectively suppressing the recombination between the photogenerated electrons and holes. Because of the high electrocatalytic activity of Ni_9S_8, the surface of the Ni_9S_8 nanostructure can also be used as the active site for electron reduction reaction, effectively reducing H^+ to H_2 in the solution. In addition, triethanolamine can absorb the holes transferred from the valence band to the surface of g-C_3N_4, thus completing a complete set of redox reactions.

4. Conclusion

A interesting g-C_3N_4/Ni_9S_8 composite was prepared by using a novel hydrothermal method. Under visible light irradiation, the optimal g-C_3N_4/Ni_9S_8 nanocomposite has high photocatalytic activity. The hydrogen evolution rate of the optimal g-C_3N_4/Ni_9S_8 composite prepared with the Ni/g-C_3N_4 feed molar ratio of 0.2 could reach 355.7 $\mu mol \cdot g^{-1} \cdot h^{-1}$ at 7 °C, which is 21.2 times higher than the raw g-C_3N_4 sample, and only 22.1% less than the raw g-C_3N_4 with Pt (1 wt.%) loaded. The possible mechanism of photocatalytic H_2 evolution over the as-acquired g-C_3N_4/Ni_9S_8 composite was that: due to the close contact between g-C_3N_4 and Ni_9S_8 of high conductivity of Ni_9S_8, the photogenerated electrons during photocatalysis could easily emigrate from the relatively low-conductivity g-C_3N_4 surface to the high-conductivity Ni_9S_8 surface, thus effectively promoting the segregation of photogenerated electrons and holes and sponsoring the electrocatalytic activity of Ni_9S_8 via effectively reducing H^+ to H_2 as well. The present study will supplied

a new approach for the construction of nano photocatalysts by co-catalysis for photocatalytic hydrogen evolution.

Declarations

Conflicts of interest

There is no conflict of interests regarding the publication of this paper.

Acknowledgements

The authors appreciate the financial support for this work from the National Natural Science Foundation of China (grant nos. 11674035 and 61274015), and the Fundamental Research Funds for the Central Universities.

References

[1] V. Ramanathan, M.V. Ramana, G. Roberts, D. Kim, C. Corrigan, C. Chung, D. Winker. Warming trends in Asia amplified by brown cloud solar absorption. Nature 448 (2007) 575-U5.

[2] G. Glenk, S. Reichelstein. Economics of converting renewable power to hydrogen. Nat. Energy 4 (2019) 212-216.

[3] A. Fujishima, K. Honda. Electrochemical photolysis of water at a semiconductor electrode. Nature 238 (1972) 37-38.

[4] L. Buzzetti, G.E.M. Crisenza, P. Melchiorre. Mechanistic studies in photocatalysis. Angew. Chem. Int. Ed. 58 (2019) 3730-3747.

[5] Y.R. Li, J. Xu, Z.Y. Liu, H. Yu. Performance of amorphous CoS_x/oxygen vacancies ZnO heterojunction photocatalytic hydrogen evolution. J. Mater. Sci. Mater. Electron. 30 (2020) 246-258.

[6] X. Wang, Q. Xu, M.R.Li, S. Shen, X.L. Wang, Y.C. Wang, Z.C. Feng, J.Y. Shi, H.X. Han, C.P. Li. Photocatalytic overall water splitting promoted by an alpha-beta phase junction on Ga_2O_3. Angew. Chem. Int. Ed. 51 (2012) 13089-13092.

[7] S.F. Wang, H.J. Gao, X.L. Yu, S.N. Tang, Y. Wang, L.M. Fang, X.X. Zhao, J.Y. Li, L. Yang, W.Q. Dang . Nanostructured SrTiO(3) with different morphologies achieved by mineral acid-assisted hydrothermal method with enhanced optical, electrochemical, and photocatalytic performances. J. Mater. Sci. Mater. Electron. 31 (2020) 17736-17754.

[8] P. Zhang, B.Y. Guan, L. Yu, X.W. Lou. Facile synthesis of multi-shelled ZnS-CdS cages with enhanced photoelectrochemical performance for solar energy conversion. CHEM 4 (2018) 162-173.

[9] S.D. Guan, X.L. Fu, Y. Zhang, Z.J. Peng. β-NiS modified CdS nanowires for photocatalytic H_2 evolution with exceptionally high efficiency. Chem. Sci. 6 (2018) 1574-1585.

[10] G. Mahalakshmi, M. Rajeswari, P. Ponnarasi. Fabrication of dandelion clock-inspired preparation of core-shell TiO_2@MoS_2 composites for unprecedented high visible light-driven photocatalytic performance. J. Mater. Sci. Mater. Electron. 31 (2020) 22252-22264.

[11] D. Chen, Z.F. Liu, Z.G. Guo, W.G. Yan, M.N. Ruan. Decorating Cu_2O photocathode with noble-metal-free Al and NiS cocatalysts for efficient photoelectrochemical water splitting by light harvesting management and charge separation design. Chem. Eng. J. 381 (2020) 122655.

[12] W.J. Ong, L.L. Tan, Y.H. Ng, S.T. Yong, S.P. Chai. Graphitic carbon nitride (g-C_3N_4)-based photocatalysts for artificial photosynthesis and environmental remediation: Are we a step closer to achieving sustainability? Chem. Rev. 116 (2016) 7159-7329.

[13] X.C. Wang, K. Maeda, A. Thomas, K. Takanabe, G. Xin, J.M. Carlsson, K. Domen, M. Antonietti. A metal-free polymeric photocatalyst for hydrogen production from water under visible light. Nat. Mater. 8 (2009) 76-80.

[14] D. Masih, Y.Y. Ma, S.G. Rohani. Graphitic C_3N_4 based noble-metal-free photocatalyst systems: A review. Appl. Catal. B 206 (2017) 556-588.

[15] C. Prasad, H. Tang, Q.Q. Liu, I. Bahadur, S. Karlapudi, Y.J. Jiang. A latest overview on photocatalytic application of g-C_3N_4 based nanostructured materials for hydrogen production. Int. J. Hydrog. Energy 45 (2020) 337-379.

[16] L.J. Zhang, X.Q. Hao, Y.B. Li, Z.L. Jin. Performance of WO_3/g-C_3N_4 heterojunction composite boosting with NiS for photocatalytic hydrogen evolution. Appl. Surf. Sci. 499 (2020).

[17] Z.W. Zhao, Y.J. Sun, F. Dong. Graphitic carbon nitride based nanocomposites: a review. Nanoscale 7 (2015) 15-37.

[18] S.D. Guan, X.L. Fu, Y. Zhang, Z.J. Peng. β-NiS modified CdS nanowires for photocatalytic H_2 evolution with exceptionally high efficiency. Chem. Sci. 6 (2018) 1574-1585.

[19] Y. Zhang, Z.J. Peng, S.D. Guan, X.L. Fu. Novel beta-NiS film modified CdS nanoflowers heterostructure nanocomposite: Extraordinarily highly efficient photocatalysts for hydrogen evolution. Appl. Catal. B 224 (2018) 1000-1008.

[20] J.H. Lee, S.I. Kim, S.M. Park, M. Kang. A p-n heterojunction NiS-sensitized TiO_2 photocatalytic system for efficient photoreduction of carbon dioxide to methane. Ceram. Int. 43 (2017) 1768-1774.

[21] K.L. He, J. Xie, M.L. Li, X. Li. In situ one-pot fabrication of g-C_3N_4 nanosheets/NiS cocatalyst heterojunction with intimate interfaces for efficient visible light photocatalytic H_2 generation. Appl. Surf. Sci. 430 (2018) 208-217.

[22] M.A. Ashraf, Y.F. Yang, A. Fakhri. Synthesis of NiS-MoO_3 nanocomposites and decorated on graphene oxides for heterogeneous photocatalysis, antibacterial and antioxidant activities. Ceram. Int. 46 (2020) 8379-8384.

[23] S.D. Guan, X.L. Fu, Z.Z. Lao, C.H. Jin, Z.J. Peng. NiS-MoS_2 Hetero-nanosheet arrays on carbon cloth for high-performance flexible hybrid energy storage devices. ACS Sustain. Chem. Eng. 7 (2019) 11672-11681.

[24] A. Khalil, Q. Liu, Z. Muhammad, M. Habib, R. Khan, Q. He, Q. Fang, H.T. Masood, Z.U. Rehman, T. Xiang, C.Q. Wu, L. Song. Synthesis of Ni_9S_8/MoS_2 heterocatalyst for enhanced hydrogen evolution reaction. Langmuir 33 (2017) 5148-5153.

[25] A. Li, Z.J. Peng, X.L. Fu. Exfoliated, mesoporous $W_{18}O_{49}$/g-C_3N_4 composites for efficient photocatalytic H_2 evolution. Solid State Sci. 106 (2020) 106298.

[26] L. F. Cui, X. Ding, Y. G. Wang, H. C. Shi, L. H. Huang, Y. H. Zuo, S. F. Kang. Facile preparation of Z-scheme WO_3/g-C_3N_4 composite photocatalyst with enhanced photocatalytic performance under visible light. Appl. Surf. Sci. 391 (2017) 202-210.

[27] P. Wang, N. Lu, Y. Su, N. Liu, H.T. Yu, J. Li, Y. Wu. Fabrication of WO_3@g-C_3N_4 with core@shell nanostructure for enhanced photocatalytic degradation activity under visible light. Appl. Surf. Sci. 423 (2017) 197-204.

[28] J.J. Huang, C.M. Gui, H.D. Ma, P. Li, W.P. Wu, Z.M. Chen. Surface metallization of PET sheet: Fabrication of Pd nanoparticle/polymer brush to catalyze electroless nickel plating. Compos. Sci. Technol. 202 (2021) 108547.

[29] H. Jung, T. T. Pham, E. W. Shin. Interactions between ZnO nanoparticles and amorphous g-C_3N_4 nanosheets in thermal formation of g-C_3N_4/ZnO composite materials: the annealing temperature effect. Appl. Surf. Sci. 458 (2018) 369-381.

Figures

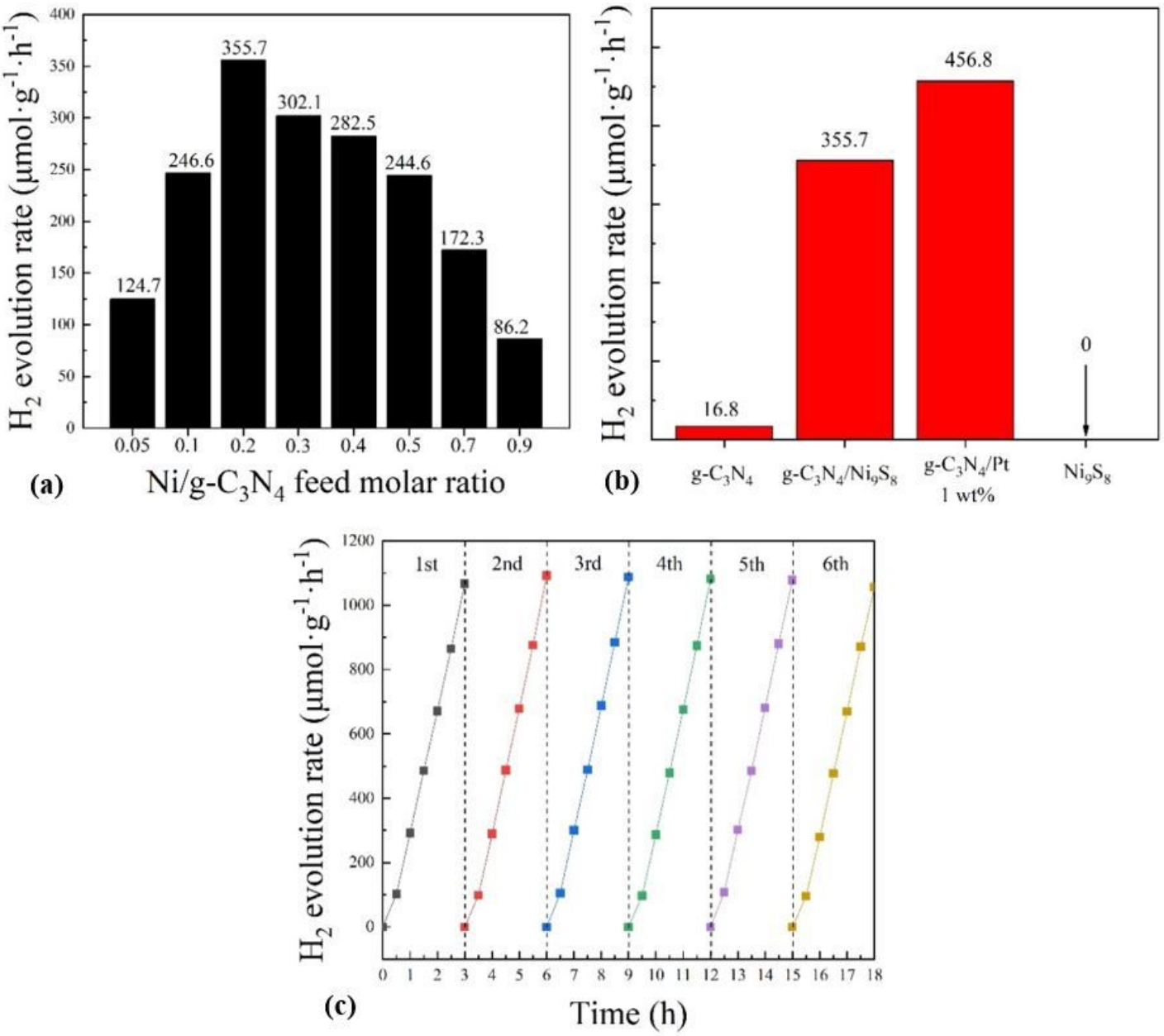

Figure 1

Photocatalytic performance on hydrogen evolution: (a) the composites prepared with different Ni/g-C3N4 feed ratios, (b) comparison on raw g-C3N4, pure Ni9S8, 1 wt.% Pt coated g-C3N4 by light deposition and the optimal g-C3N4/Ni9S8 sample, and (c) the cycling tests on the optimal g-C3N4/Ni9S8 composite. The photocatalytic reactions were carried out with 20 mg catalyst, 100 ml aqueous solution containing 10 vol% TEOA and a 300 W Xe lamp with UV cut-off filter (λ ≥ 420 nm).

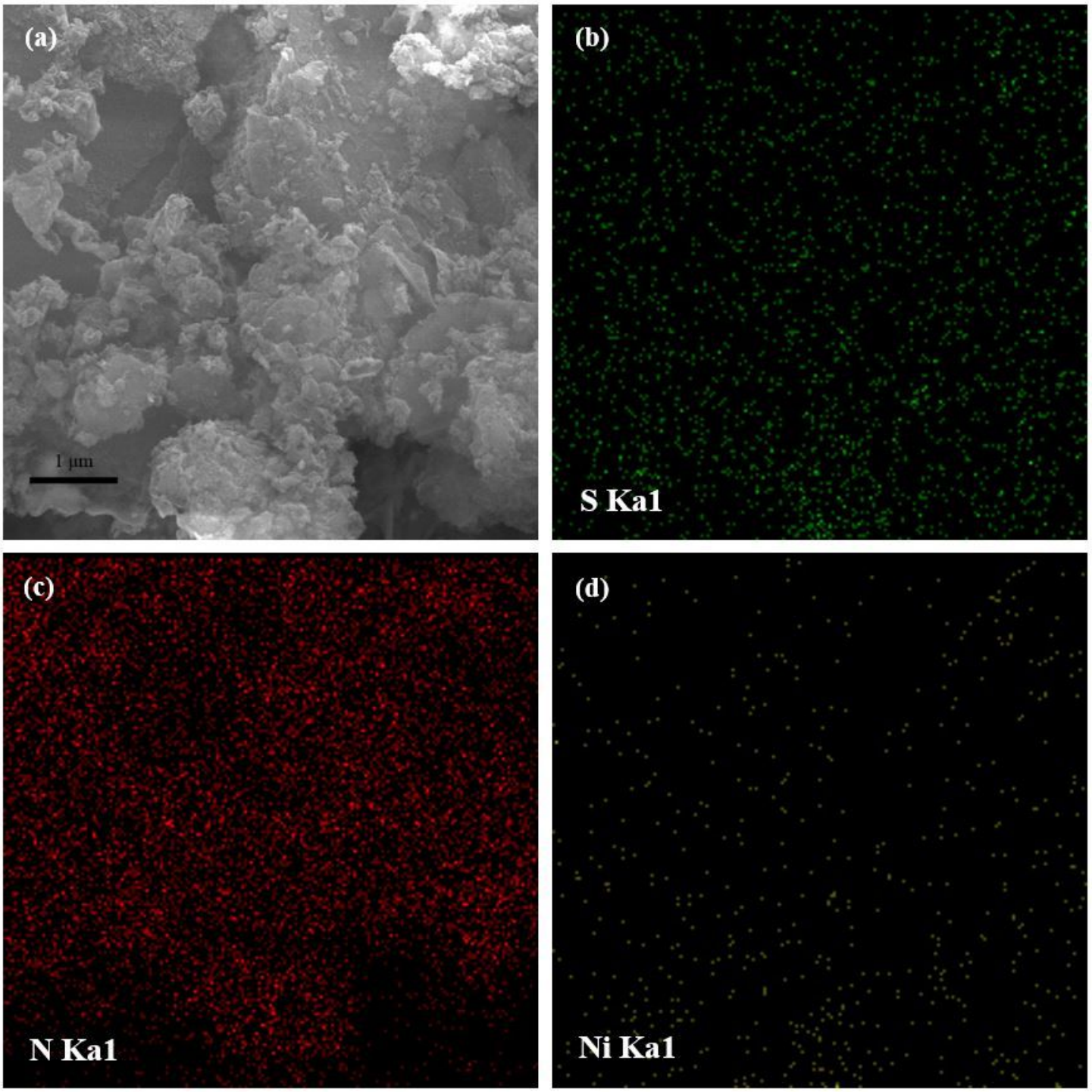

Figure 2

Microstructure and mainly elemental distribution of the optimal sample: (a) SEM image, and EDS mapping images of (b) S, (c) N, (d) Ni.

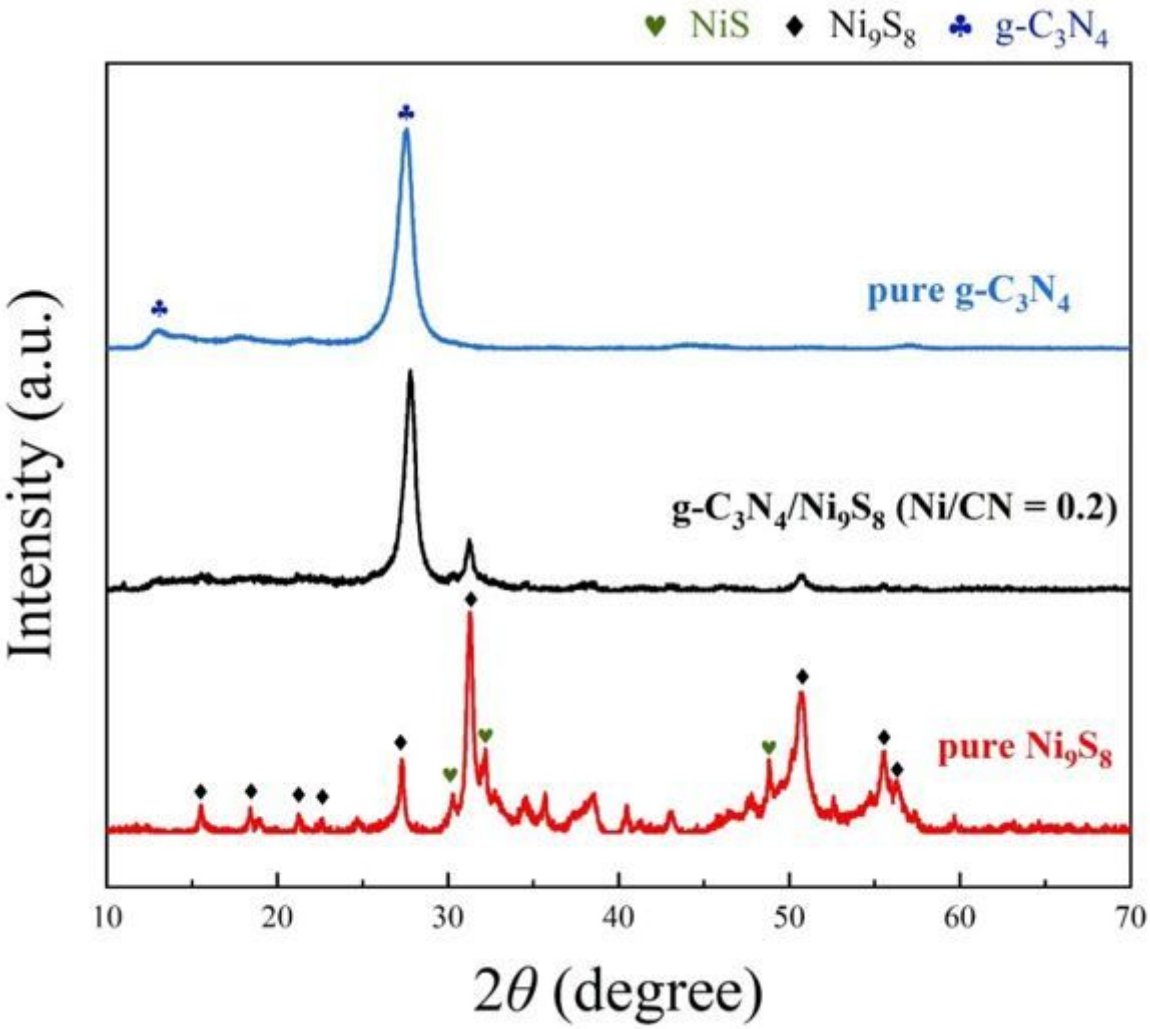

Figure 3

XRD patterns of the optimal g-C3N4/Ni9S8 composite, raw g-C3N4 and pure nickel sulfides samples.

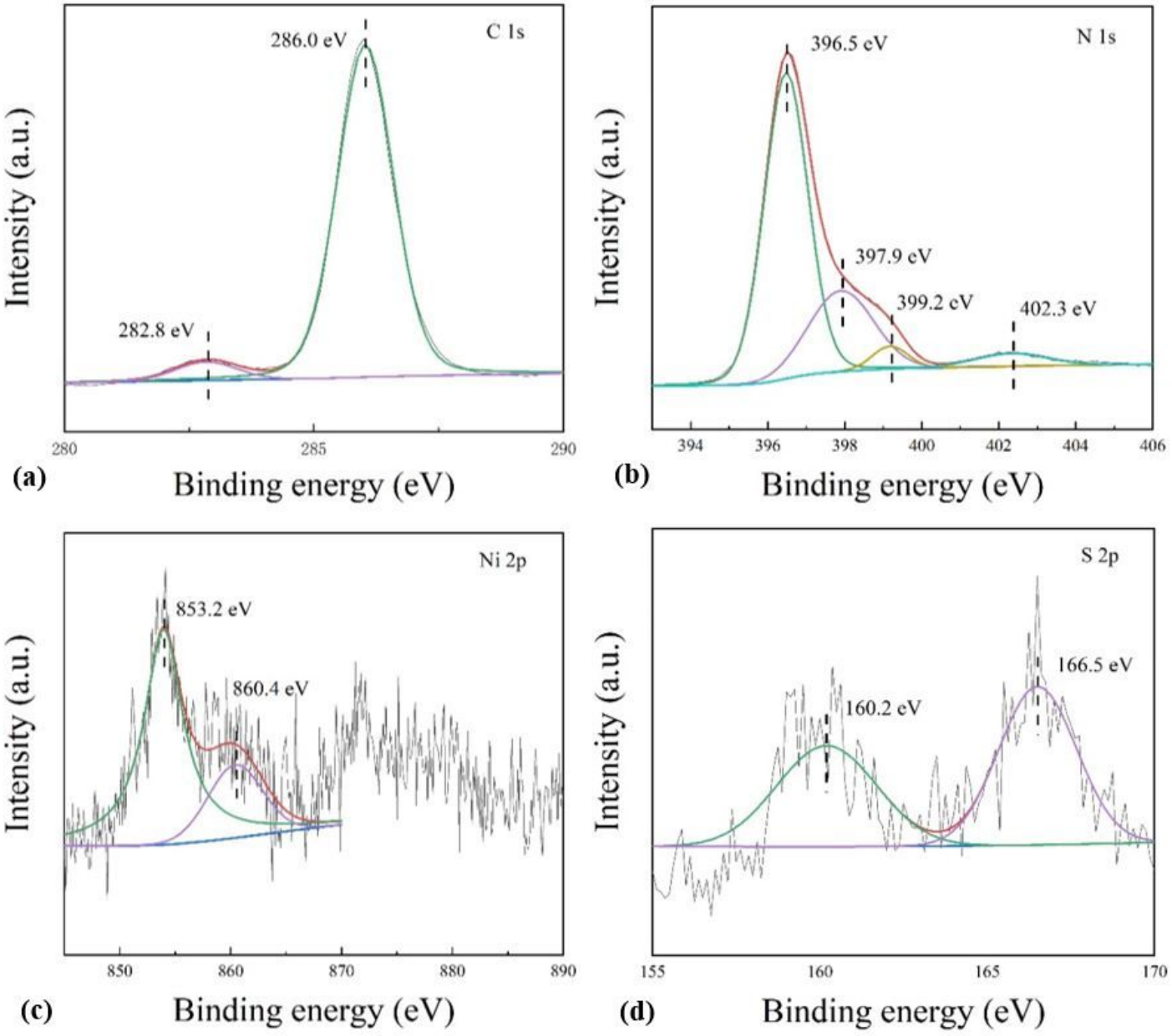

Figure 4

High resolution XPS spectra of (a) C 1s, (b) N 1s, (c) Ni 2p and (d) S 2p in the obtained g-C3N4/Ni9S8 composite.

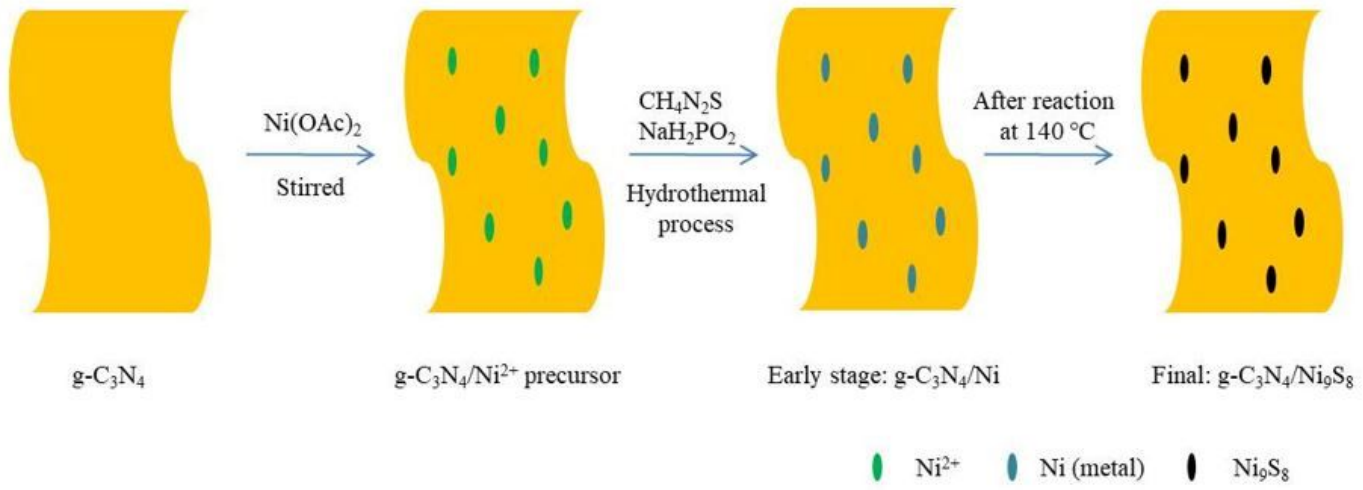

Figure 5

Mechanism of the present g-C3N4/Ni9S8 composite

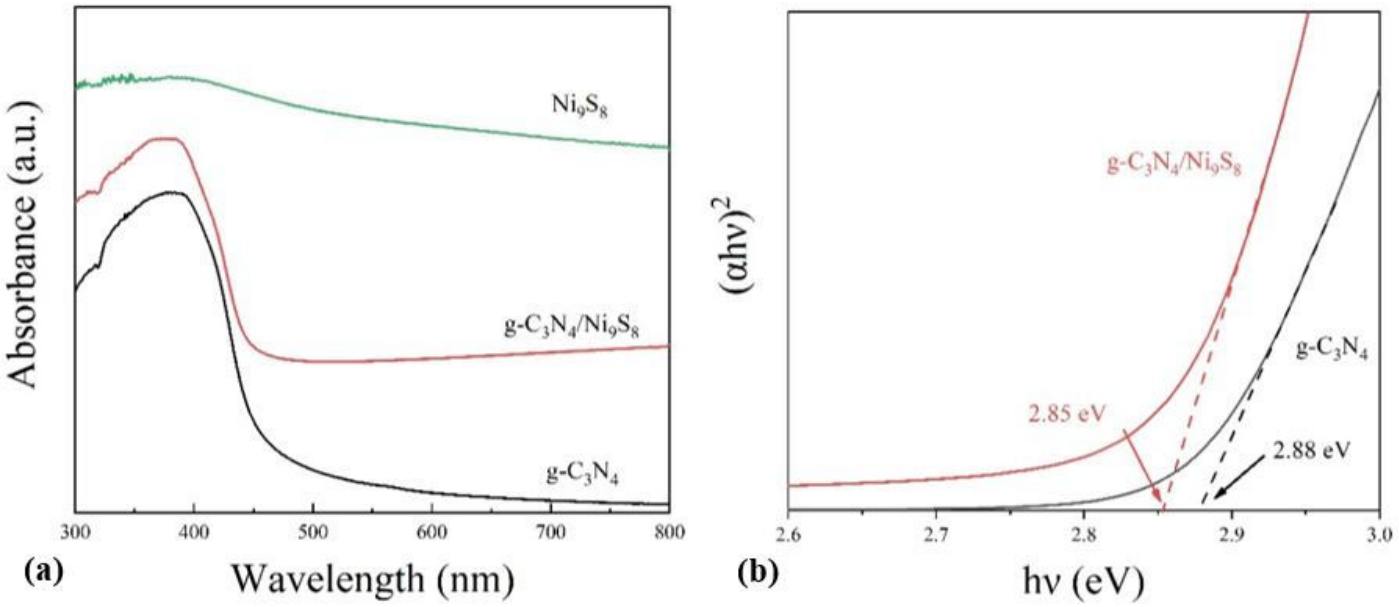

Figure 6

Optical properties: (a) UV-Vis absorption spectra (b) and the corresponding (ahv)2 versus Eg plots of the optimal g-C3N4/Ni9S8 composite, raw g-C3N4 and Ni9S8.

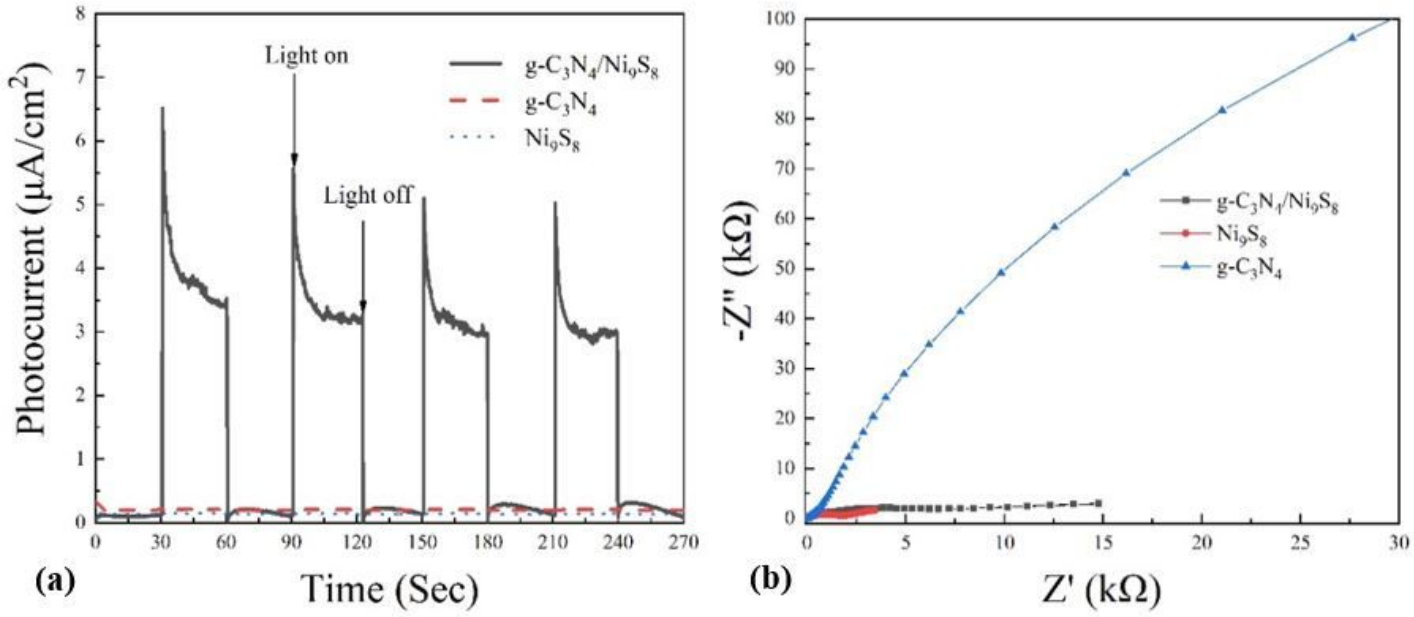

Figure 7

Photoelectrochemical data of the optimal g-C3N4/Ni9S8 composite, raw g-C3N4 and pure Ni9S8 nanostructure: (a) transient photocurrent responses, and (b) EIS Nyquist plots.

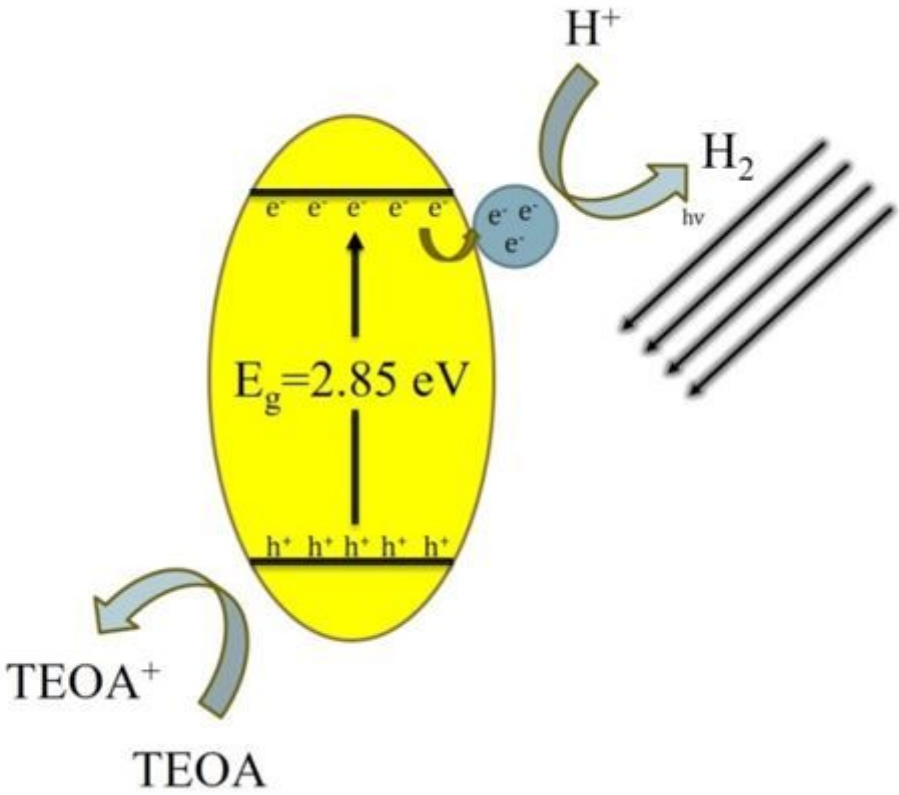

Figure 8

Photocatalytic Mechanism for hydrogen evolution over the optimal g-C3N4/Ni9S8 composite.